

---

# JPEG INSPIRED DEEP LEARNING

Ahmed H. Salamah\*, Kaixiang Zheng\*, Yiwen Liu & En-Hui Yang

Department of Electrical and Computer Engineering, University of Waterloo

{ahamsalamah, k56zheng, e3liu, ehyang}@uwaterloo.ca

## ABSTRACT

Although it is traditionally believed that lossy image compression, such as JPEG compression, has a negative impact on the performance of deep neural networks (DNNs), it is shown by recent works that well-crafted JPEG compression can actually improve the performance of deep learning (DL). Inspired by this, we propose JPEG-DL, a novel DL framework that prepends any underlying DNN architecture with a trainable JPEG compression layer. To make the quantization operation in JPEG compression trainable, a new differentiable soft quantizer is employed at the JPEG layer, and then the quantization operation and underlying DNN are jointly trained. Extensive experiments show that in comparison with the standard DL, JPEG-DL delivers significant accuracy improvements across various datasets and model architectures while enhancing robustness against adversarial attacks. Particularly, on some fine-grained image classification datasets, JPEG-DL can increase prediction accuracy by as much as 20.9%. Our code is available on <https://github.com/JpegInspiredDl/JPEG-Inspired-DL.git>.

## 1 INTRODUCTION

JPEG compression (Pennebaker & Mitchell, 1992) is the *defacto* lossy image compression technique with ubiquitous presence in real-world applications. With the development of deep learning, more and more images, potentially compressed by JPEG, are consumed by deep neural networks (DNNs). Naturally, it's of interest to study how JPEG compression will impact DNN performance for computer vision tasks, and extensive research has been conducted along this line such as Dodge & Karam (2016); Liu et al. (2018) and Xie & Kim (2019). These initial explorations establish a widely accepted view that the information loss caused by JPEG obscures important features in the input image, thereby negatively impacting DNN performance.

However, it was shown in Yang et al. (2021) that the above conventional wisdom does not hold anymore if JPEG compression is applied intelligently and adaptively on a per image basis. Indeed, Yang et al. (2021) showed that if applied appropriately, JPEG compression can actually improve DNN performance at least in theory. They further proposed to train a DNN based on images with various JPEG quality levels. While they managed to demonstrate improved performance with a specially designed DNN topology, the model is too cumbersome to be fully trained, leading to suboptimal performance. Moreover, the adherence to the default JPEG quantization also limits the effectiveness of this method. On the other hand, given a fixed DNN model, Zheng et al. (2023) and Salamah et al. (2024b) found that its performance could be slightly improved if the input images got compressed by JPEG with optimized quantization parameters. However, the performance gain is not significant due to the frozen DNN model. Although these existing works provide promising insights to improve DNN performance with JPEG compression, a solid solution that can fully unleash the potential of this idea has yet to be found.

---

\* Authors contributed equally.

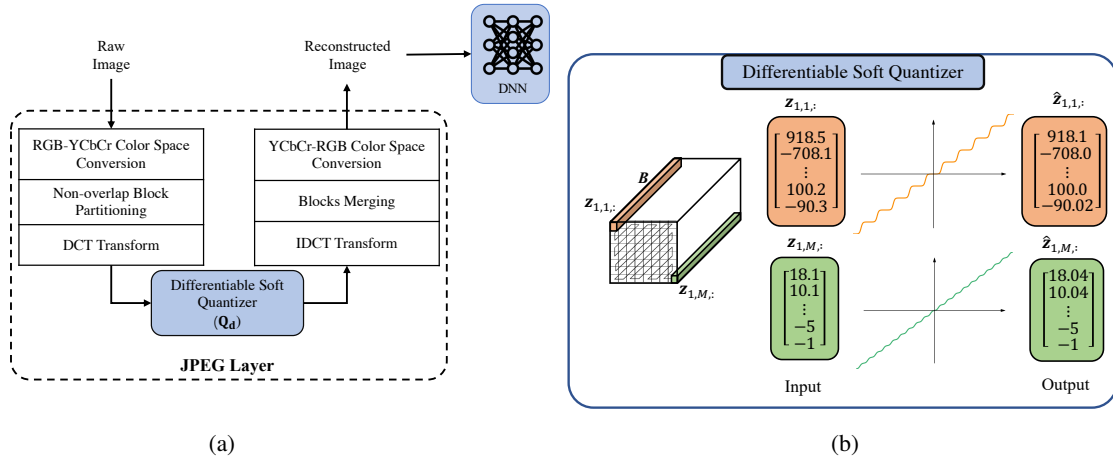


Figure 1: (a) The JPEG-DL framework is illustrated, with the forward and inverse processes of the standard JPEG pipeline shown in white boxes as non-trainable operations. The differentiable soft quantizer ( $Q_d$ ) and the underlying DNN architecture, shown in blue, represent the only trainable components. (b) As an example, we show  $z_{1,:}$ , i.e., the DCT representation of the Y channel of an image, by a tensor consisting of  $B$  blocks of DCT coefficients. Each  $8 \times 8$  block contains  $M = 64$  DCT frequencies, ordered from low to high in a zigzag manner. Then, we show how  $z_{1,1,:}$  and  $z_{1,M,:}$  are quantized by  $Q_d(\cdot; q = 1, \alpha = 10)$  and  $Q_d(\cdot; q = 0.5, \alpha = 16)$ , respectively.

To address the above issue, in this paper, we propose jointly optimizing both JPEG quantization operation and a DNN to achieve greater effectiveness. To this end, we first introduce a trainable JPEG compression layer, structure of which is illustrated in Fig. 1a. This layer follows the standard JPEG pipeline to convert a raw input image into blockwise Discrete Cosine Transform (DCT) coefficients in the YCbCr color space. A novel differentiable soft quantizer ( $Q_d$ ) is then applied to quantize the DCT coefficients at each frequency position, followed by the standard JPEG inverse process to reconstruct the RGB image. We then present JPEG-DL, a novel deep learning (DL) framework that integrates the trainable JPEG layer at the input side of the DL pipeline. This layer can be regarded as an additional layer prefixed to any underlying DNN architecture, whose parameters get optimized jointly with DNN model weights during training. The core of JPEG-DL is  $Q_d$  as it substitutes the non-differentiable, hard quantization in JPEG with a differentiable, soft quantization operation defined by a neat analytical formula, which not only facilitates gradient-based optimization for quantization parameters but also introduces additional trainable non-linearity to the overall image understanding pipeline. To validate the effectiveness of JPEG-DL, we conducted extensive experiments for image classification on six datasets including four fine-grained classification datasets (Wah et al., 2011; Khosla et al., 2011; Nilsback & Zisserman, 2008; Parkhi et al., 2012), CIFAR-100 (Krizhevsky et al., 2009) and ImageNet (Deng et al., 2009). Results show that JPEG-DL significantly and consistently outperforms the standard DL across various DNN architectures, with a negligible increase in model complexity. Specifically, JPEG-DL improves classification accuracy by up to 20.9% on some fine-grained classification dataset, while adding only 128 trainable parameters to the DL pipeline. Moreover, the superiority of JPEG-DL over the standard DL is further demonstrated by the enhanced adversarial robustness of the learned models and reduced file sizes of the input images.

The main contributions of this paper can be summarized as follows:

- 
- We introduce a novel trainable JPEG layer leveraging differentiable soft quantizers with nice analytical formulas.
  - Based on the new JPEG layer, we propose a new DL framework dubbed JPEG-DL, which jointly optimizes the JPEG layer and the DNN model during training.
  - The outstanding performance of JPEG-DL over the standard DL is verified by comprehensive experimental results on various image classification datasets across multiple DNN architectures and for a variety of tasks including adversarial defense and data compression.

## 2 BACKGROUND AND RELATED WORK

**JPEG applications.** JPEG was originally developed as a lossy image compression technique based on transform coding, which reduces image file sizes by generating their compact representations. Beyond its traditional use, JPEG has found numerous applications in deep learning: (1) it has been utilized as a data augmentation technique to improve robustness of DNNs against image compression (Benbarrad et al., 2022); (2) it has been employed as an empirical defense method against adversarial attacks, effectively reducing adversarial perturbations and enhancing the adversarial robustness of DNNs (Dziugaite et al., 2016; Das et al., 2017; Guo et al., 2018); and (3) it has been integrated into the knowledge distillation (Hinton et al., 2015) framework by Salamah et al. (2024a), where it helps the teacher model transfer knowledge to the student model in a more effective way. In contrast, this paper focuses on leveraging JPEG to enhance the natural performance, instead of the robust performance, of DNNs without relying on any teacher model.

**Optimizing JPEG Compression for DNN vision.** As a lossy image compression technique, JPEG is developed specifically for the human visual system. As a result, while the information loss introduced by JPEG is often imperceptible to humans, it can significantly degrade the performance of DNNs. This issue gives rise to a line of research which optimizes JPEG compression based on DNN perception. For instance, given a pretrained DNN, Xie & Kim (2019), Zheng et al. (2023) and Salamah et al. (2024b) first derive its sensitivity to different DCT frequencies, based on which they customize JPEG quantization tables for this DNN to reach the optimal rate-accuracy tradeoff. Another popular direction is to make JPEG trainable, which integrates the JPEG encoder and DNN into an end-to-end differentiable training framework (Luo et al., 2020; Xie et al., 2022). These methods create differentiable proxies for image quantization and bitrate calculation, so that JPEG compression can be optimized via backpropagation in order to minimize a total loss considering both DNN performance and bitrate. However, all the above works focus on mitigating DNN performance degradation in the presence of JPEG compressed images, but offer little to no improvement on DNN performance when raw images are given as input. On the contrary, this paper leverages JPEG purely as a tool to improve DNN performance on raw images, regardless of its compression capability.

**Improving DNN performance with JPEG.** Due to the aforementioned reason, JPEG compression generally hurts DNN performance. However, it’s recently demonstrated by Yang et al. (2021) that, with an oracle guiding the compression process, one can select an optimal quality level to compress each image, enabling the DNN to make its best possible prediction for it. By applying this adaptive JPEG compression across a set of images, one can actually improve the DNN prediction accuracy considerably. This phenomenon, termed “compression helps” in the original paper, is justified by the fact that compression can remove noise and disturbing background features, thereby highlighting the main object in an image, which helps DNNs make better prediction. Due to the need of ground truth labels in the compression stage, the above adaptive compression scheme is not realizable in most real world applications; however, the discovery of “compression helps” at least show the potential of using JPEG to improve DNN performance. Thus motivated, the authors in turn proposed an implementable way to improve DNN performance with JPEG. They built a new DNN topology that incorporates 11 parallel branches of an underlying pretrained model, with each branch obtaining as input either the raw image or its compressed version at a varying quality level. The penultimate layer representations from all branches are concatenated and fed into a classification head, which is then trained

together with those 11 model backbones as a unified DNN structure. This new DNN topology is clearly too complex to train, so the authors opted for partial training to mitigate the training complexity, therefore resulting in a suboptimal performance. In contrast, our proposed method introduces only 128 additional trainable parameters to the existing DL pipeline, causing negligible complexity increase. Moreover, it’s noteworthy that our method is orthogonal to theirs, as our trainable JPEG quantization tables can be embedded into their framework to replace the default JPEG quantization tables, thereby further improving the performance.

**Trainable Activation Functions.** Relentless efforts have been made to search for activation functions that can improve DNN performance. Among all the directions, trainable activation functions have gained particular interest for their flexibility, expressive power, and adaptability during training. Chen & Chang (1996) propose the adjustable generalized hyperbolic tangent function, which extends the classic hyperbolic tangent function by introducing parameters to control the saturation level and slope of the function. He et al. (2015) introduce the parametric ReLU (PReLU), a variant of ReLU with a trainable parameter that adjusts the negative part of ReLU. More recently, Kolmogorov-Arnold Networks (KANs) (Liu et al., 2024) employ trainable activation functions on edges, with nodes simply summing all the incoming activations. Interestingly, the differentiable soft quantizers in our JPEG layer can be interpreted as trainable activation functions whose input is the DCT representations of images. These trainable soft quantizers effectively introduce additional nonlinearity to DNN models, thus improving their expressive power.

### 3 JPEG-DL: JPEG INSPIRED DL

#### 3.1 PROBLEM FORMULATION

In the JPEG pipeline, an RGB image  $x$  is first converted to the YCbCr color space and then partitioned into  $B$  non-overlapping  $8 \times 8$  blocks, where DCT is applied to each of these blocks to obtain the corresponding DCT coefficients. For each color channel, the DCT coefficients in each block are then flattened following the zigzag order, resulting in  $M = 64$  frequency positions ordered from low frequency to high frequency. Therefore, we denote the DCT coefficients of the image  $x$  as  $z = [z_{l,m,n}]$ , where  $l = 1, 2, 3$  corresponds to the color channel Y, Cb and Cr respectively,  $1 \leq m \leq M$  is the index for frequency position, and  $1 \leq n \leq B$  is the index for block. Up to this point, all operations involved are differentiable. Next, quantization tables  $Q_Y = [q_1, q_2, \dots, q_M]$  and  $Q_C = [q_{M+1}, q_{M+2}, \dots, q_{2M}]$  are used for the luminance (Y) and chrominance (CbCr) channels respectively to quantize their DCT coefficients. Following uniform quantization, we obtain quantized DCT coefficients  $\hat{z}_{l,m,n} = \lfloor z_{l,m,n}/q_m \rfloor \cdot q_m$  for  $l = 1$ , and  $\hat{z}_{l,m,n} = \lfloor z_{l,m,n}/q_{M+m} \rfloor \cdot q_{M+m}$  for  $l = 2, 3$ . Note that quantization is non-differentiable due to the use of the rounding operation. Finally, inverse operations including blockwise inverse DCT (IDCT) transform, blocks merging and YCbCr-to-RGB color space conversion are conducted over  $\hat{z}$  sequentially to obtain the reconstructed RGB image  $\hat{x}$ . Similar to their forward counterparts, all these inverse operations are differentiable. Denoting the composition of all the above operations as  $\mathcal{J}$ , we then have  $\hat{x} = \mathcal{J}(x; Q)$ , where  $Q = (Q_Y, Q_C)$ . Hereafter, the mapping  $\mathcal{J}$  stands for the JPEG encoding-decoding operation.

In supervised learning, each  $x \in \mathcal{X}$  corresponds to a ground truth label  $y \in \mathcal{Y}$ . Let  $f_\theta$  represent a DNN model with trainable weights  $\theta$ , and let  $\mathcal{L}$  denote the loss function used to train this DNN. In standard DL, the primary objective is to solve the following minimization problem:

$$\min_{\theta} \mathbb{E}[\mathcal{L}(f_\theta(x), y)]. \tag{1}$$

In contrast, JPEG-DL tries to improve the performance of DNN by jointly training it with the JPEG operation. As a result, the formulation should be instead:

$$\min_{\theta, Q} \mathbb{E}[\mathcal{L}(f_\theta(\mathcal{J}(x; Q)), y)]. \tag{2}$$

However, in order to solve (2) with gradient descent, the key challenge is caused by the non-differentiable quantization operation, which makes the gradients w.r.t.  $Q$  almost zero everywhere. To address this issue,

we will introduce a *differentiable soft quantizer* ( $Q_d$ ) in the next subsection, replacing the uniform quantizer ( $Q_u$ ) used in  $\mathcal{J}$ .

### 3.2 DIFFERENTIABLE SOFT QUANTIZER

Denote the index set of uniform quantization as

$$\mathcal{A} = \{-L, -L + 1, \dots, 0, \dots, L - 1, L\}. \quad (3)$$

For convenience,  $\mathcal{A}$  is also regarded as a vector of length  $2L + 1$ . Multiplying  $\mathcal{A}$  with a quantization step size  $q$ , we get the corresponding reconstruction space

$$\hat{\mathcal{A}} = q \times [-L, -L + 1, \dots, 0, \dots, L - 1, L]. \quad (4)$$

Again, we will regard  $\hat{\mathcal{A}}$  as both a vector and a set.

To randomly quantize a DCT coefficient  $z$  to an element in  $\hat{\mathcal{A}}$ , we invoke from Yang & Hamidi (2024) a trainable conditional probability mass function (CPMF)  $P_\alpha(\cdot|z)$  over the reconstruction space  $\hat{\mathcal{A}}$  or equivalently the index set  $\mathcal{A}$  given  $z$ , where  $\alpha > 0$  is a trainable parameter:

$$P_\alpha(iq|z) = \frac{e^{-\alpha(z-iq)^2}}{\sum_{j \in \mathcal{A}} e^{-\alpha(z-jq)^2}}, \forall i \in \mathcal{A}. \quad (5)$$

Extend  $z$  to a vector of length  $2L + 1$ , i.e.,  $[z]_{2L+1} = [\overbrace{z, \dots, z}^{2L+1 \text{ times}}]$ . Then, the CPMF  $P_\alpha(\cdot|z)$ , regarded as a vector of length  $2L + 1$ , can be easily computed via the softmax operation  $\sigma(\cdot)$ :

$$[P_\alpha(\cdot|z)]_{2L+1} = \sigma\left(-\alpha \times \left([z]_{2L+1} - \hat{\mathcal{A}}\right)^2\right). \quad (6)$$

With the CPMF  $P_\alpha(\cdot|z)$ ,  $z$  is now quantized to each  $iq \in \hat{\mathcal{A}}$  with probability  $P_\alpha(iq|z)$ . Note that as  $\alpha \rightarrow \infty$ ,  $P_\alpha(\cdot|z)$  approaches an one-hot vector with probability 1 at the nearest point to  $z$  in  $\hat{\mathcal{A}}$  and 0 elsewhere. Therefore, the resulting random quantizer effectively functions as the deterministic uniform quantizer  $Q_u(z) = \lfloor z/q \rfloor \cdot q$ .

Based on the CPMF  $P_\alpha(\cdot|z)$ , we can now define a differentiable soft quantizer  $Q_d$  as the conditional expectation of  $iq$  given  $z$ , i.e.,

$$Q_d(z) = \mathbb{E}[iq|z] = \sum_{i \in \mathcal{A}} P_\alpha(iq|z) \cdot iq. \quad (7)$$

Similarly, as  $\alpha \rightarrow \infty$ ,  $Q_d$  also goes to  $Q_u$ . Fig. 2 shows how the shape of  $Q_d$  varies w.r.t  $\alpha$ , given a fixed  $q$ .

This soft quantizer  $Q_d$  serves as an analytical proxy for  $Q_u$ . It's differentiable everywhere, allowing gradients to flow through it smoothly. More importantly, compared to  $Q_u$ ,  $Q_d$  involves a trainable parameter  $\alpha$  which can adjust the softness of the quantizer, thereby introducing more flexibility. In view of these nice properties,  $Q_d$  is the ideal candidate in place of  $Q_u$  used in  $\mathcal{J}$ .

As a side note, for the reader who is not familiar with quantization, but familiar with the attention operation used in transformer models (Vaswani, 2017),  $Q_d$  can be regarded as an attention operation in broad sense, with the query being  $z$ , the key and value being  $\hat{\mathcal{A}}$ , and the similarity metric between the query and key being negative squared distance instead of dot product.

### 3.3 OVERALL FRAMEWORK OF JPEG-DL

Substituting  $Q_u$  in  $\mathcal{J}$  with  $Q_d$ , we get a differentiable JPEG layer  $\hat{\mathcal{J}}$  parameterized by  $Q$  and  $\alpha$ , where  $\alpha = (\alpha_Y, \alpha_C)$ .  $\alpha_Y = [\alpha_1, \alpha_2, \dots, \alpha_M]$  and  $\alpha_C = [\alpha_{M+1}, \alpha_{M+2}, \dots, \alpha_{2M}]$  are  $\alpha$  tables for the luminance and chrominance channels respectively, used in conjunction with  $Q_Y$  and  $Q_C$  to quantize DCT coefficients. Following the proposed soft quantization, we obtain quantized DCT coefficients  $\hat{z}_{l,m,n} = Q_d(z_{l,m,n}; q_m, \alpha_m)$  for  $l = 1$ , and  $\hat{z}_{l,m,n} = Q_d(z_{l,m,n}; q_{M+m}, \alpha_{M+m})$  for  $l = 2, 3$ , where  $Q_d(z; q, \alpha)$  denotes a differentiable soft quantizer defined in (7) parameterized by a quantization step  $q$  and a scaling factor  $\alpha$ . Overall, for an input image  $x$ , we have  $\hat{x} = \hat{\mathcal{J}}(x; Q, \alpha)$ . Therefore, we can rewrite (2), the JPEG-DL formulation, as

$$\min_{\theta, Q, \alpha} \mathbb{E}[\mathcal{L}(f_{\theta}(\hat{\mathcal{J}}(x; Q, \alpha)), y)], \quad (8)$$

where the expectation can be approximated by the empirical mean over a mini-batch in actual training. Thanks to the use of  $Q_d$ , (8) can now be solved by gradient descent with ease (see Appendix A.1 for the derivative analytical formulas).

After training with JPEG-DL, we get the optimized parameters  $\theta^*$ ,  $Q^*$  and  $\alpha^*$ . Then, we consider the composition of the JPEG layer and the underlying DNN as a unified DNN model  $\hat{f}(x; \theta^*, Q^*, \alpha^*) = f_{\theta^*}(\hat{\mathcal{J}}(x; Q^*, \alpha^*))$  to do validation. Concretely, any raw input  $x$  should be fed into  $\hat{\mathcal{J}}$ , instead of directly to  $f_{\theta^*}$ , thus allowing the reconstructed image  $\hat{x}$  to be fed into the underlying DNN  $f_{\theta^*}$ . In other words, the JPEG layer is prepended as the first layer of any underlying DNN.

To conclude this section, we refer readers to Fig. 1a and Fig. 1b for an illustration of the inner workings of the JPEG-DL framework.

## 4 EXPERIMENTS

**CIFAR-100.** We evaluate our proposed method using a transformer-based architecture and four state-of-the-art convolutional neural networks (CNNs): EfficientFormer-L1 (Li et al., 2022), ResNet (He et al., 2016), VGG (Simonyan & Zisserman, 2014), MobileNet (Sandler et al., 2018), and ShuffleNet (Ma et al., 2018). For ResNet, we employ CIFAR-specific versions: ResNet32, ResNet56, and ResNet110. For VGG, we utilize VGG8 and VGG13. All CNN architectures follow the training recipe from CRD (Tian et al., 2020) (see Appendix A.3), while for the transformer-based architecture, EfficientFormer-L1, we adhere to the setup proposed by Xu et al. (2023) (see Appendix A.5).

**Fine-grained Tasks.** These tasks involve visually similar classes and typically feature fewer training samples per class compared to conventional classification tasks. We evaluate our method on four datasets: CUB-200-2011 (Wah et al., 2011), Stanford Dogs (Khosla et al., 2011), Flowers (Nilsback & Zisserman, 2008), and Pets (Parkhi et al., 2012). For CNN architectures, we employ PreAct ResNet-18 (He et al., 2016)

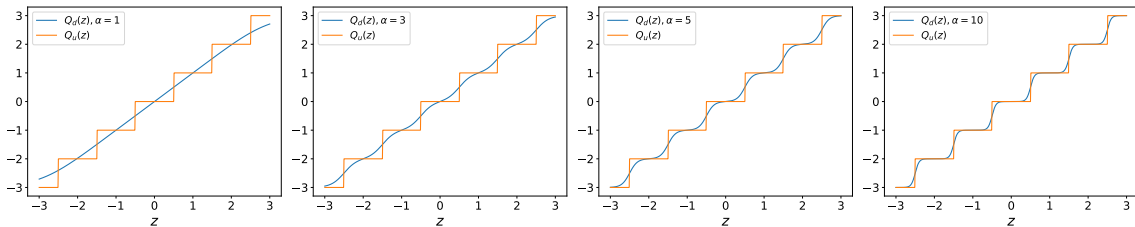


Figure 2: Illustration of  $Q_u$  vs.  $Q_d$  with  $\alpha = 1, 3, 5, 10$ , where  $L$  and  $q$  are set to 3 and 1, respectively.

and DenseNet-BC (Huang et al., 2017), following the experimental setup and architecture modifications of Zhang et al. (2017). For the transformer-based architecture, we use EfficientFormer-L1, adopting the setup outlined by Xu et al. (2023) (see Appendices A.4 and A.5).

**JPEG-layer settings** for CIFAR-100 and fine-grained tasks. Given the gradient nature of  $Q_d$ , as demonstrated in Appendix A.1.1,  $q$  for different DCT frequencies shows varying magnitudes at a fixed  $\alpha$ , resulting in differing gradient magnitudes. To address this, we use the ADAM optimizer to adapt the learning rate for each  $q$  in our JPEG layer across the tested models, enabling more efficient training and better convergence. Moreover, we explore the gradient behavior of  $Q_d$  with respect to  $\alpha$ . Our analysis in Appendix A.1.2 shows that when  $\alpha$  is decently large such that  $Q_d$  is not too far away from  $Q_u$ , the gradient magnitude is almost zero for  $\alpha$ . This indicates that  $\alpha$  won't be updated effectively as long as we initialize it within a decent range. Experiments also confirmed that training  $\alpha$  won't cause a significant change in model performance. As a result, we choose not to train over  $\alpha$  in our framework. For CIFAR-100, set the learning rate to 0.003 across all tested models. For the fine-grained datasets, set the JPEG learning rate to 0.005. Across these datasets, we fix  $\alpha_m = 5$  for all  $1 \leq m \leq 2M$ , and set  $L = 2^{b-1}$  in (3), where  $b$  is a tunable hyperparameter and set to 8.

**ImageNet-1K.** For all experiments on this dataset, we utilize the standard training recipes shown by Paszke et al. (2019) without any modifications. We use SqueezeNet (Iandola, 2016), ResNet-18 and ResNet-34 as our testing underlying models.

**JPEG-layer settings** for ImageNet-1K. We will utilize specific settings to control the gradient magnitude to ensure more stable updates for  $Q$ . We define the Gradient Scaling Constants  $\tilde{h}_m = \alpha_m q_m^2$ ,  $1 \leq m \leq 2M$ , which allows us to control the magnitude of gradients w.r.t  $Q$ . Specifically, we fixed  $\tilde{h}_m = 0.7$  for all  $1 \leq m \leq 2M$ . During training, we update the value of  $\alpha_m$  to be  $\tilde{h}_m/q_m^2$  before calculating the gradients w.r.t  $Q$ . As a result of controlling the maximum gradient magnitude, we can optimize  $Q$  using an SGD optimizer with 0.5 learning rate, instead of an ADAM optimizer. This approach ensures stable and efficient training for quantization table updates (see Appendix A.2 for more details). For this dataset,  $b$  is equal to 11 across all tested models.

**Quantization Table Initialization.** For CIFAR-100 and fine-grained tasks, we initialize the quantization table  $Q$  based on the reciprocal of sensitivity for each DCT frequency, given a pre-trained model of the underlying DNN architecture, following the approach described by Zheng et al. (2023); Salamah et al. (2024b). Broadly speaking, the sensitivity of a frequency indicates the rate of change of the loss function w.r.t. the perturbation on this frequency, so we favor a smaller quantization step for a more sensitive frequency to limit the distortion amount on it. For ImageNet-1K, we adopt the strategy from Esser et al. (2019), where the initialization of  $q_m$  is based on the average of absolute values of DCT coefficients across all blocks in all training images that will be quantized by  $q_m$ . Specifically,  $q_m = 2 \sum_{k=1}^N \sum_{n=1}^B |z_{1,m,n}^{(k)}| / (NB\sqrt{2^{b-1}})$  for  $1 \leq m \leq M$ , i.e.  $Q_Y$ , and  $q_m = \sum_{k=1}^N \sum_{l=2}^3 \sum_{n=1}^B |z_{l,m,n}^{(k)}| / (NB\sqrt{2^{b-1}})$  for  $M+1 \leq m \leq 2M$ , i.e.,  $Q_C$ , where  $k$  is the index for image and  $N$  is the number of training images.

Table 1: Top-1 validation accuracy (%) for Baseline and JPEG-DL on CIFAR-100. The Baseline results are from Tian et al. (2020). For JPEG-DL, we report the mean and standard deviation of experimental results over three runs.

Method	Res32	Res56	Res110	VGG8	VGG13	MobileNetV2	ShuffleNetV2
Baseline	71.14	72.34	73.79	70.36	73.77	64.6	71.82
JPEG-DL	<b>71.92</b> $\pm$ 0.31 (+0.78)	<b>73.39</b> $\pm$ 0.19 (+1.05)	<b>74.46</b> $\pm$ 0.11 (+0.67)	<b>71.10</b> $\pm$ 0.41 (+0.74)	<b>75.32</b> $\pm$ 0.10 (+1.55)	<b>65.91</b> $\pm$ 0.11 (+1.31)	<b>73.04</b> $\pm$ 0.16 (+1.22)

**Results.** For CIFAR-100 and fine-grained tasks, the performance of JPEG-DL is shown in Tables 1 and 2. Across all seven tested models for CIFAR-100, JPEG-DL consistently provides improvements, with gains of up to 1.53% in top-1 accuracy. In the fine-grained tasks, JPEG-DL offers a substantial performance increase,

Table 2: Top-1 validation accuracy (%) on various fine-grained image classification tasks and model architectures. We report the mean and standard deviation of experimental results over three runs.

Model	Method	CUB-200	Dogs	Flowers	Pets
ResNet-18	Baseline	54.00 $\pm$ 1.43	63.71 $\pm$ 0.32	57.13 $\pm$ 1.28	70.37 $\pm$ 0.84
	JPEG-DL	<b>58.81</b> $\pm$ 0.12 (+4.81)	<b>65.57</b> $\pm$ 0.37 (+1.86)	<b>68.76</b> $\pm$ 0.57 (+11.63)	<b>74.84</b> $\pm$ 0.66 (+4.47)
DenseNet-121	Baseline	57.70 $\pm$ 0.44	66.61 $\pm$ 0.17	51.32 $\pm$ 0.57	70.26 $\pm$ 0.79
	JPEG-DL	<b>61.32</b> $\pm$ 0.43 (+3.62)	<b>69.67</b> $\pm$ 0.58 (+3.06)	<b>72.22</b> $\pm$ 1.05 (+20.90)	<b>75.90</b> $\pm$ 0.68 (+5.64)

Table 3: Top-1 validation accuracy (%) on ImageNet with different model architectures.

Method	SqueezeNetV1.1	Resnet18	Resnet34
Baseline	57.95	69.75	73.31
JPEG-DL	<b>58.26</b> (+0.31)	<b>70.13</b> (+0.38)	<b>73.54</b> (+0.23)

with improvements of up to 20.90% across all datasets using two different models. More results for CIFAR-100 and fine-grain tasks using a transformer-based model are shown in Appendix A.5. For ImageNet-1K, the performance of JPEG-DL is shown in Table 3. With a trivial increase in complexity (adding 128 parameters), JPEG-DL achieves a gain of 0.31% in top-1 accuracy for SqueezeNetV1.1 compared to the baseline using a single round of  $Q_d$  quantization operation. By increasing the number of quantization rounds to five, we observe an additional improvement of 0.20%, leading to a total gain of 0.51% over the baseline. The best results are indicated in bold, and values in parentheses indicate relative accuracy gains over the baseline.

## 5 ANALYSIS AND DISCUSSION

**Robustness.** JPEG has generally been used as an empirical defense mechanism against adversarial attacks by mitigating adversarial perturbations and enhancing the robustness of DNNs, as discussed in Section 2. To evaluate the adversarial robustness of JPEG-DL models in comparison to standard DNN, we conduct experiments using two attack methods, FGSM and PGD, on CIFAR-100 with two different models from Table 1. The perturbation budget, Epsilon, ranged from 1 to 4 for both attack methods. For PGD, we applied 5 steps with a perturbation step size of  $(2.5 \times \text{Epsilon})/\text{steps}$ , following the setup used by Madry (2017). As shown in Fig. 3, the JPEG-DL models significantly improve the adversarial robustness compared to the standard DNN models, with improvements of up to 15% for FGSM and 6% for PGD.

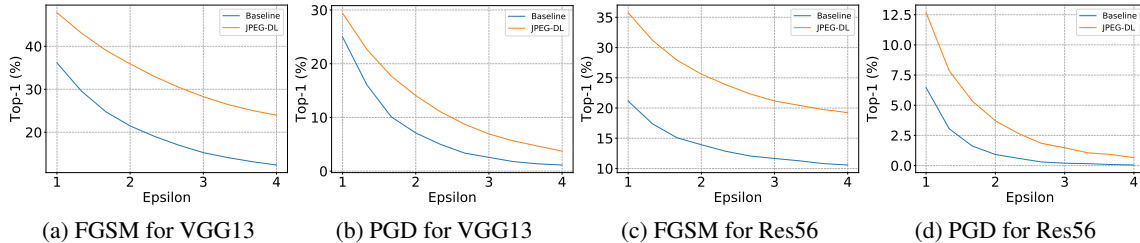


Figure 3: Evaluate the adversarial robustness of JPEG-DL models in comparison to standard DNN on VGG13 and Res56 for CIFAR-100 against FGSM and PGD attacks.

**Ablation study between  $Q_d$  and  $Q_u$ .** In our JPEG-DL framework, we employ  $Q_d$  in the JPEG layer  $\hat{\mathcal{J}}(x; Q, \alpha)$  to introduce differentiability into the JPEG framework. As illustrated in Fig. 2, we know that  $Q_d$  is close to  $Q_u$  given a decently large  $\alpha$ . So, we are curious to see if we can replace  $Q_d$  in  $\hat{\mathcal{J}}$  with

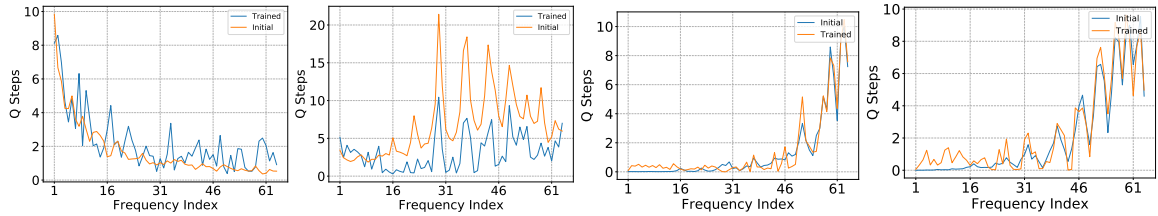


$Q_u$  during validation, where we don’t need differentiability. The application of  $Q_u$  has a great advantage that DCT coefficients are quantized into a discrete alphabet such that they can be effectively compressed by entropy coding, e.g. Huffman coding. Therefore, it’s potential that we can achieve both compression and accuracy improvement simultaneously! Thus motivated, we evaluate both the top-1 validation accuracy and the compression rate after replacing  $Q_d$  with  $Q_u$ . This ablation study is conducted on the same models used in Table 2 across all fine-grained datasets. The results, summarized in Table 4, show that  $Q_u$  achieves almost the same performance gains as  $Q_d$ , with a compression ratio of up to 2.92x. These findings confirm that  $Q_d$  is sufficiently hard for quantization when  $\alpha$  is large, while still preserving the advantages of both model performance and compression. We will show some examples of the quantization tables used in this ablation study in the next subsection.

Table 4: Ablation study comparing  $Q_d$  and  $Q_u$  on various fine-grained datasets and model architectures listed in Table 2. For both  $Q_u$  and  $Q_d$ , validation accuracy and performance gains relative to their baseline are shown in parentheses. For  $Q_u$ , the compression rate is reported, with the compression ratio calculated as 24 divided by the compression rate, also shown in parentheses. Results are averaged over three runs.

Model	Method	CUB-200	Dogs	Flowers	Pets
ResNet-18	$Q_d$ (%)	58.81 (+4.81)	65.58 (+1.87)	68.76 (+11.63)	74.85 (+4.48)
	$Q_u$ (%)	58.81 (+4.81)	65.55 (+1.84)	68.79 (+11.66)	74.86 (+4.49)
	Rate (bpp)	11.71 (2.05x)	8.29 (2.89x)	10.96 (2.19x)	12.98 (1.85x)
DenseNet-121	$Q_d$ (%)	61.33 (+3.63)	69.67 (+3.06)	72.22 (+20.90)	75.90 (+5.64)
	$Q_u$ (%)	61.31 (+3.61)	69.66 (+3.05)	72.09 (+20.77)	75.77 (+5.51)
	Rate (bpp)	11.45 (2.10x)	8.63 (2.78x)	8.22 (2.92x)	12.26 (1.96x)

**Designed Quantization Tables.** Fig. 4 presents the Y and CbCr quantization tables, both at initialization and after convergence, for VGG13 trained on CIFAR-100 and ResNet-18 trained on the CUB200 dataset. The estimated sensitivity values used to initialize these quantization tables are provided in Appendix A.6.



(a) VGG13 (Y Channel) (b) VGG13 (CbCr Channel) (c) ResNet-18(Y Channel) (d) ResNet-18 (CbCr Channel)

Figure 4: Initial and final quantization tables for VGG13 trained on CIFAR-100 and ResNet18 trained on CUB200, with frequency indices arranged in the default zigzag order.

**Feature maps visualization.** Fig. 5 presents the feature maps extracted after the first dense block in DenseNet-121 for both the JPEG-DL model and the baseline model, trained on the CUB200 dataset using the model from Table 2. The output of the feature maps at this stage is of size  $56 \times 56$ , and both sets are shown in the same sequence using the same original image. The shown example was incorrectly classified by the baseline model, while the JPEG-DL model correctly classified it. In this figure, it is evident that the feature maps from the JPEG-DL model show significantly better contrast between the foreground information (the bird) and the background compared to the feature maps generated by the baseline model. Specifically, the foreground object in the JPEG-DL feature maps is enclosed within a well-defined contour, making it visually distinguishable from the background. In contrast, the baseline model’s feature maps show a more blended structure, where the foreground contains higher energy in low frequencies, causing it to

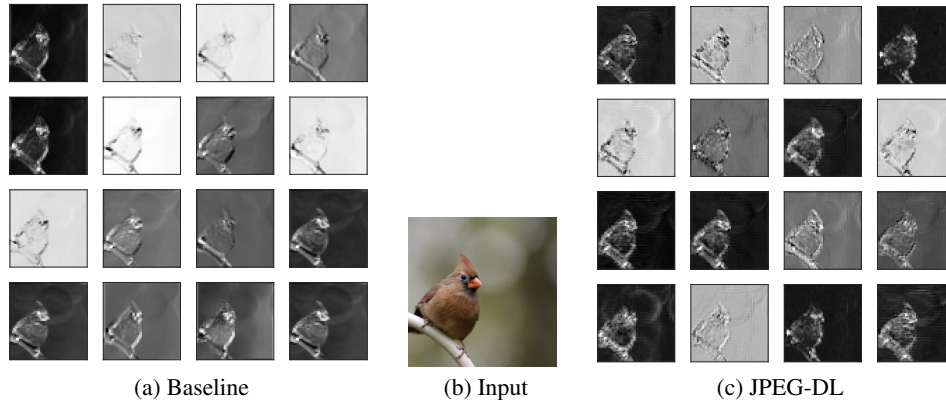


Figure 5: Feature maps of size  $56 \times 56$  are shown after the first dense block in DenseNet-121 for both JPEG-DL and baseline models Figs. in 5a and 5c, respectively, using an original input shown in Fig.5b. The JPEG-DL model highlights the foreground (bird) more distinctly, while the baseline model shows less contrast, contributing to its misclassification.

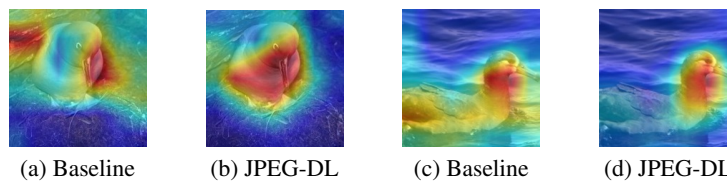


Figure 6: GradCAM++ visualization for baseline and JPEG-DL models on CUB200 using two examples, where the baseline model incorrectly classified them and the JPEG-DL model correctly classified them.

blend more smoothly with the background. Additionally, another example in Appendix A.7 shows a similar phenomenon in addition to background information being more effectively removed, following the same setup as the first example. These discrepancies in feature map clarity and contrast are propagated through subsequent blocks of DenseNet-121, eventually contributing to the misclassification problem observed in the baseline model.

**Interpretability using CAM.** Fig. 6 illustrates GradCAM++ visualizations (Chattopadhyay et al., 2018) for two examples from the CUB-200 dataset, comparing the baseline model with JPEG-DL using ResNet-18 as our underlying model. In both instances, the baseline model incorrectly classifies the input, while the JPEG-DL model correctly classifies it. The visualizations highlight how JPEG-DL focuses more precisely on the main object in the image, demonstrating the model’s improved attention to key regions that contribute to correct classification. This highlights the effectiveness of JPEG-DL in enhancing model interpretability and performance, and it also supports the case for background removal discussed in the previous subsection.

## 6 CONCLUSION

In contrast to the conventional understanding that JPEG compression negatively impacts the DL performance, this paper introduces a novel trainable JPEG compression layer into the DL pipeline to improve DL performance, termed JPEG-DL. This layer enables gradient-based optimization for quantization parameters and can be integrated seamlessly with any underlying DNN to be trained jointly. To validate the

---

effectiveness of JPEG-DL, we conduct extensive experiments on six image classification datasets and show significant gain over the standard DL. Additionally, we demonstrate that JPEG-DL improves the adversarial robustness of the learned model, and can also be used to reduce input image file sizes.

---

## REFERENCES

- Tajeddine Benbarrad, Salaheddine Kably, Mounir Arioua, and Nabih Alaoui. Compression-based data augmentation for cnn generalization. In *International Conference on Cybersecurity, Cybercrimes, and Smart Emerging Technologies*, pp. 235–244. Springer, 2022.
- Aditya Chattopadhyay, Anirban Sarkar, Prantik Howlader, and Vineeth N Balasubramanian. Grad-cam++: Generalized gradient-based visual explanations for deep convolutional networks. In *2018 IEEE winter conference on applications of computer vision (WACV)*, pp. 839–847. IEEE, 2018.
- Chyi-Tsong Chen and Wei-Der Chang. A feedforward neural network with function shape autotuning. *Neural networks*, 9(4):627–641, 1996.
- Nilaksh Das, Madhuri Shanbhogue, Shang-Tse Chen, Fred Hohman, Li Chen, Michael E. Kounavis, and Duen Horng Chau. Keeping the bad guys out: Protecting and vaccinating deep learning with jpeg compression. *ArXiv*, abs/1705.02900, 2017.
- Jia Deng, Wei Dong, Richard Socher, Li-Jia Li, Kai Li, and Li Fei-Fei. ImageNet: A large-scale hierarchical image database. In *2009 IEEE conference on computer vision and pattern recognition*, pp. 248–255. Ieee, 2009.
- Samuel Dodge and Lina Karam. Understanding how image quality affects deep neural networks. In *2016 eighth international conference on quality of multimedia experience (QoMEX)*, pp. 1–6. IEEE, 2016.
- Gintare Karolina Dziugaite, Zoubin Ghahramani, and Daniel M. Roy. A study of the effect of JPG compression on adversarial images. *CoRR*, abs/1608.00853, 2016.
- Steven K Esser, Jeffrey L McKinstry, Deepika Bablani, Rathinakumar Appuswamy, and Dharmendra S Modha. Learned step size quantization. *arXiv preprint arXiv:1902.08153*, 2019.
- Chuan Guo, Mayank Rana, Moustapha Cisse, and Laurens van der Maaten. Countering adversarial images using input transformations. In *International Conference on Learning Representations*, 2018.
- Kaiming He, Xiangyu Zhang, Shaoqing Ren, and Jian Sun. Delving deep into rectifiers: Surpassing human-level performance on imagenet classification. In *Proceedings of the IEEE international conference on computer vision*, pp. 1026–1034, 2015.
- Kaiming He, Xiangyu Zhang, Shaoqing Ren, and Jian Sun. Deep residual learning for image recognition. In *Proceedings of the IEEE conference on computer vision and pattern recognition*, pp. 770–778, 2016.
- Geoffrey Hinton, Oriol Vinyals, Jeff Dean, et al. Distilling the knowledge in a neural network. *arXiv preprint arXiv:1503.02531*, 2(7), 2015.
- Gao Huang, Zhuang Liu, Laurens Van Der Maaten, and Kilian Q Weinberger. Densely connected convolutional networks. In *Proceedings of the IEEE conference on computer vision and pattern recognition*, pp. 4700–4708, 2017.
- Forrest N Iandola. Squeezenet: Alexnet-level accuracy with 50x fewer parameters and; 0.5 mb model size. *arXiv preprint arXiv:1602.07360*, 2016.
- Aditya Khosla, Nityananda Jayadevaprakash, Bangpeng Yao, and Fei-Fei Li. Novel dataset for fine-grained image categorization: Stanford dogs. In *Proc. CVPR workshop on fine-grained visual categorization (FGVC)*, volume 2. Citeseer, 2011.
- Alex Krizhevsky, Geoffrey Hinton, et al. Learning multiple layers of features from tiny images. 2009.

- 
- Yanyu Li, Geng Yuan, Yang Wen, Eric Hu, Georgios Evangelidis, Sergey Tulyakov, Yanzhi Wang, and Jian Ren. Efficientformer: Vision transformers at mobilenet speed. *arXiv preprint arXiv:2206.01191*, 2022.
- Zihao Liu, Tao Liu, Wujie Wen, Lei Jiang, Jie Xu, Yanzhi Wang, and Gang Quan. DeepN-JPEG: A deep neural network favorable JPEG-based image compression framework. In *Proceedings of the 55th Annual Design Automation Conference*, pp. 18. ACM, 2018.
- Ziming Liu, Yixuan Wang, Sachin Vaidya, Fabian Ruele, James Halverson, Marin Soljačić, Thomas Y Hou, and Max Tegmark. Kan: Kolmogorov-arnold networks. *arXiv preprint arXiv:2404.19756*, 2024.
- Xiyang Luo, Hossein Talebi, Feng Yang, Michael Elad, and Peyman Milanfar. The rate-distortion-accuracy tradeoff: Jpeg case study. *arXiv preprint arXiv:2008.00605*, 2020.
- Ningning Ma, Xiangyu Zhang, Hai-Tao Zheng, and Jian Sun. Shufflenet v2: Practical guidelines for efficient cnn architecture design. In *Proceedings of the European conference on computer vision (ECCV)*, pp. 116–131, 2018.
- Aleksander Madry. Towards deep learning models resistant to adversarial attacks. *arXiv preprint arXiv:1706.06083*, 2017.
- Maria-Elena Nilsback and Andrew Zisserman. Automated flower classification over a large number of classes. In *2008 Sixth Indian conference on computer vision, graphics & image processing*, pp. 722–729. IEEE, 2008.
- Omkar M Parkhi, Andrea Vedaldi, Andrew Zisserman, and CV Jawahar. Cats and dogs. In *2012 IEEE conference on computer vision and pattern recognition*, pp. 3498–3505. IEEE, 2012.
- Adam Paszke, Sam Gross, Francisco Massa, Adam Lerer, James Bradbury, Gregory Chanan, Trevor Killeen, Zeming Lin, Natalia Gimelshein, Luca Antiga, et al. Pytorch: An imperative style, high-performance deep learning library. *Advances in neural information processing systems*, 32, 2019.
- William B. Pennebaker and Joan L. Mitchell. *JPEG Still Image Data Compression Standard*. Kluwer Academic Publishers, Norwell, MA, United States, 1992. ISBN 0442012721.
- Ahmed H Salamah, Shayan Mohajer Hamidi, and En-Hui Yang. A coded knowledge distillation framework for image classification based on adaptive jpeg encoding. *Pattern Recognition*, pp. 110966, 2024a.
- Ahmed H Salamah, Kaixiang Zheng, Linfeng Ye, and En-Hui Yang. Jpeg compliant compression for dnn vision. *IEEE Journal on Selected Areas in Information Theory*, 2024b.
- Mark Sandler, Andrew Howard, Menglong Zhu, Andrey Zhmoginov, and Liang-Chieh Chen. Mobilenetv2: Inverted residuals and linear bottlenecks. In *Proceedings of the IEEE conference on computer vision and pattern recognition*, pp. 4510–4520, 2018.
- Karen Simonyan and Andrew Zisserman. Very deep convolutional networks for large-scale image recognition. *arXiv preprint arXiv:1409.1556*, 2014.
- Yonglong Tian, Dilip Krishnan, and Phillip Isola. Contrastive representation distillation. In *International Conference on Learning Representations*, 2020.
- A Vaswani. Attention is all you need. *Advances in Neural Information Processing Systems*, 2017.
- Catherine Wah, Steve Branson, Peter Welinder, Pietro Perona, and Serge Belongie. The caltech-ucsd birds-200-2011 dataset. 2011.

- 
- Xiufeng Xie and Kyu-Han Kim. Source compression with bounded dnn perception loss for iot edge computer vision. In *The 25th Annual International Conference on Mobile Computing and Networking*, pp. 1–16, 2019.
- Xiufeng Xie, Ning Zhou, Wentao Zhu, and Ji Liu. Bandwidth-aware adaptive codec for dnn inference offloading in iot. In *European Conference on Computer Vision*, pp. 88–104. Springer, 2022.
- Zhiqiu Xu, Yanjie Chen, Kirill Vishniakov, Yida Yin, Zhiqiang Shen, Trevor Darrell, Lingjie Liu, and Zhuang Liu. Initializing models with larger ones. In *The Twelfth International Conference on Learning Representations*, 2023.
- En-Hui Yang and Shayan Mohajer Hamidi. Systems and methods for training deep learning models. 2024.
- En-Hui Yang, Hossam Amer, and Yanbing Jiang. Compression helps deep learning in image classification. *Entropy*, 23(7):881, 2021.
- Hongyi Zhang, Moustapha Cisse, Yann N Dauphin, and David Lopez-Paz. mixup: Beyond empirical risk minimization. *arXiv preprint arXiv:1710.09412*, 2017.
- Kaixiang Zheng, Ahmed H. Salamah, Linfeng Ye, and En-Hui Yang. Jpeg compliant compression for dnn vision. In *2023 IEEE International Conference on Image Processing (ICIP)*, pp. 1875–1879, 2023. doi: 10.1109/ICIP49359.2023.10221982.

---

## A APPENDIX

### A.1 PARTIAL DERIVATIVES OF $Q_d$

With the CPMF  $P_\alpha(\cdot|z)$  shown in (6),  $z$  is now quantized to each  $\hat{z} \in \hat{\mathcal{A}}$  with probability  $P_\alpha(\hat{z}|z)$ . Denote this random mapping by

$$\hat{z} = Q_p(z). \quad (9)$$

Note that given  $z$ ,  $\hat{z}$  is a random variable taking values in  $\hat{\mathcal{A}}$  with distribution  $P_\alpha(\cdot|z)$ .

#### A.1.1 QUANTIZATION STEP AND INPUT

The partial derivatives of  $Q_d(z)$  w.r.t.  $q$  and  $z$  are obtained as

$$\frac{\partial Q_d(z)}{\partial z} = 2\alpha \text{Var}\{Q_p(z)\}, \quad (10a)$$

$$\begin{aligned} \frac{\partial Q_d(z)}{\partial q} &= \frac{1}{q} \left( \mathbb{E}\{Q_p(z)\} + (2\alpha z) \text{Var}\{Q_p(z)\} \right. \\ &\quad \left. - (2\alpha) \text{Skew}_u\{Q_p(z)\} \right), \end{aligned} \quad (10b)$$

where for any random variable  $V$ ,

$$\text{Skew}_u(V) \triangleq \sum_v v^3 \mathbb{P}_V(v) - \left( \sum_v v \mathbb{P}_V(v) \right) \left( \sum_v v^2 \mathbb{P}_V(v) \right).$$

#### A.1.2 SCALING FACTOR $\alpha$

The partial derivatives of  $Q_d(z)$  w.r.t.  $\alpha$  obtained as

$$\begin{aligned} \frac{\partial Q_d(z)}{\partial \alpha} &= \frac{\partial \sum_{i \in \mathcal{A}} iq P_\alpha(iq|z)}{\partial \alpha} \\ &= \sum_{i \in \mathcal{A}} iq \frac{\partial P_\alpha(iq|z)}{\partial \alpha} \end{aligned} \quad (11)$$

$$\begin{aligned} \frac{\partial P_\alpha(iq|z)}{\partial \alpha} &= \frac{-(z-iq)^2 e^{-\alpha(z-iq)^2}}{\sum_{j \in \mathcal{A}} e^{-\alpha(z-jq)^2}} + \frac{e^{-\alpha(z-iq)^2} \sum_{j \in \mathcal{A}} (z-jq)^2 e^{-\alpha(z-jq)^2}}{(\sum_{j \in \mathcal{A}} e^{-\alpha(z-jq)^2})^2} \\ &= P_\alpha(iq|z) \sum_{j \in \mathcal{A}} (z-jq)^2 P_\alpha(jq|z) - (z-iq)^2 P_\alpha(iq|z) \end{aligned} \quad (12)$$

Plugging (2) in (1) yields

$$\begin{aligned} \frac{\partial Q_d(z)}{\partial \alpha} &= \sum_{i \in \mathcal{A}} iq P_\alpha(iq|z) \sum_{j \in \mathcal{A}} (z-jq)^2 P_\alpha(jq|z) - \sum_{i \in \mathcal{A}} iq (z-iq)^2 P_\alpha(iq|z) \\ &= \mathbb{E}\{Q_p(z)\} \mathbb{E}\{(z-Q_p(z))^2\} - \mathbb{E}\{Q_p(z)(z-Q_p(z))^2\} \\ &= -\text{Cov}\{Q_p(z), (z-Q_p(z))^2\} \end{aligned} \quad (13)$$

To gain a better understanding, we fix  $q$  and  $b$ , and analyzed how  $\frac{\partial Q_d(z)}{\partial \alpha}$  behaves for different values of  $\alpha$ . From Fig. 7, it is evident that the gradient magnitude decreases as  $\alpha$  increases. This indicates that  $Q_d$  approaches the shape of the uniform quantizer  $Q_u$ , as shown previously in Fig. 2, leading to a reduction in the gradient magnitude for  $\alpha$ . As a result, when  $\alpha$  becomes sufficiently large, the gradient approaches zero, effectively preventing further updates to  $\alpha$ , making it act as a non-trainable parameter at a certain point of the training process. Based on this observation and verified experimental results, we opt not to train  $\alpha$ , as it does not impact the overall performance.

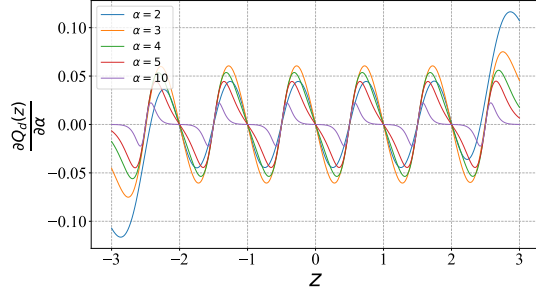


Figure 7: This Figure illustrates the partial derivatives of  $Q_d(z)$  w.r.t. the scaling factor  $\alpha$ , where  $b = 3$  and  $q = 1$ .

## A.2 GRADIENT SCALING

The partial derivatives of  $Q_d(z)$  with respect to  $q$  at a fixed value of  $\alpha$  are shown in Fig. 8a. As shown, increasing the value of  $q$  leads to an increase in the gradient magnitude. To control instability in the updates of the 128 quantization parameters in  $Q$ , we propose utilizing  $\alpha$  to control the magnitude of  $\frac{\partial Q_d(z)}{\partial q}$ . Fig. 8b demonstrates that with a fixed value of  $q$ , decreasing  $\alpha$  effectively reduces the gradient magnitude. By leveraging this control mechanism, we can stabilize the magnitude of the gradients that updates  $Q$ .

To explore the relationship between  $\alpha$  and  $q$ , we refer to the exponent in (5),  $\alpha(z - iq)^2$ , which can be rewritten by expressing  $z = cq$ , resulting in the form  $\alpha q^2(c - i)^2$ . From this, we define a new term,  $\tilde{h} = \alpha q^2$ , referred to as the *Gradient Scaling Constant*. To further illustrate this relationship, in Fig. 8b, we set  $\tilde{h} = 2$ , and by selecting different pairs of  $\alpha$  and  $q$  values, we demonstrate that the maximum magnitude of  $\frac{\partial Q_d(z)}{\partial q}$  remains invariant. This confirms that the gradient magnitude can be effectively controlled by adjusting  $\alpha$  based on the last updated value of  $q$ , according to the specified  $\tilde{h}$  value. This adjustment allows for controlled quantization updates, reducing the potential instability during training. Moreover, by controlling the gradient magnitude, we simplify the optimization process, enabling the use of a single learning rate for all  $q$  values by using the SGD optimizer, instead of the ADAM optimizer. This gradient scaling mechanism is analogous to the ADAM optimizer, which adapts different learning rates for individual trainable parameters based on momentum and recent gradient magnitudes.

## A.3 CNN-BASED SETTINGS

For CIFAR100, we deploy a stochastic gradient descent (SGD) optimizer with a momentum of 0.9, a weight decay of 0.0005, and a batch size of 64. We initialize the learning rate as 0.05, and decay it by 0.1 every 30 epochs after the first 150 epochs until the last 240 epoch. For MobileNetV2, ShuffleNetV1 and Shuf-



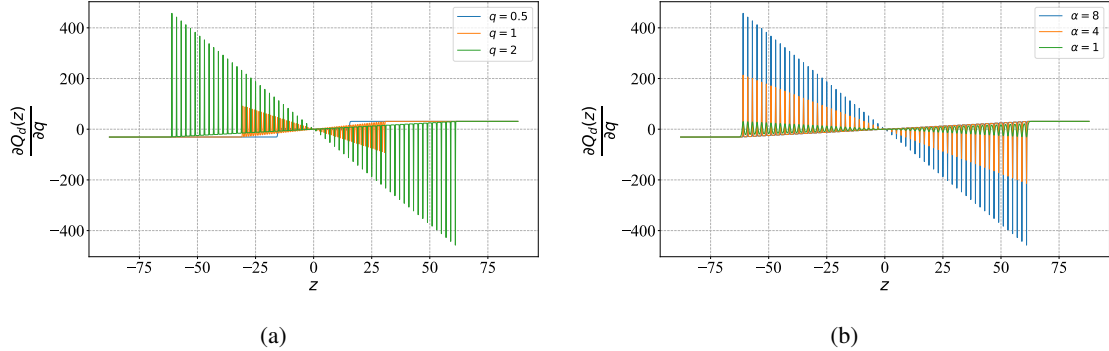


Figure 8: Figures 8a and ?? illustrate the partial derivatives of  $Q_d(z)$  w.r.t. the parameter  $q$  for cases where  $\alpha = 8$  and  $q$  varies and  $\alpha$  varies and  $q = 2$ , respectively. For both figures, we set  $b = 6$ .

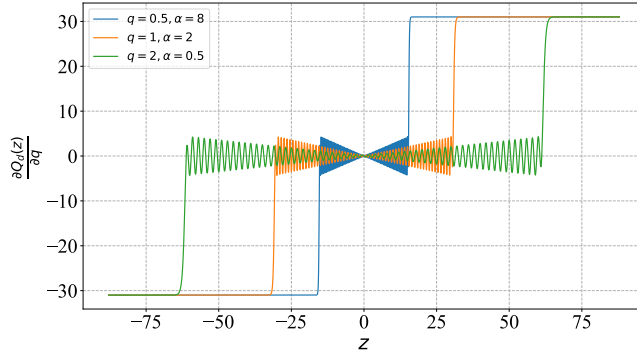


Figure 9: Demonstrating impact of  $h$  on gradient magnitude for various combinations of  $q$  and  $\alpha$ . We fixed  $h=2$  and  $b=6$ .

fleNetV2, we use a learning rate of 0.01 as this learning rate is optimal for these models in a grid search, while 0.05 is optimal for other models.

For fine-grained classification tasks, all networks are trained from scratch and optimized by SGD with a momentum 0.9, weight decay of 0.0001, and an initial learning rate of 0.1. The learning rate is divided by 10 after epochs 100 and 150 for all datasets, and the total epochs are 200. We set batch size 32 for these fine-grained classification tasks. We use the standard data augmentation technique for ImageNet (Deng et al., 2009), *i.e.*, flipping and random cropping.

#### A.4 FINE-GRAINED MODEL ARCHITECTURES

We use standard ResNet-18 with 64 filters and DenseNet-121 with a growth rate of 32 for image size  $224 \times 224$ . For fine-grained classification tasks, we use PreAct ResNet-18 (He et al., 2016), which modifies the first convolutional layer with kernel size  $3 \times 3$ , strides 1 and padding 1, instead of the kernel size  $7 \times 7$ , strides 2 and padding 3, for image size  $32 \times 32$  by following Zhang et al. (2017). We use DenseNet-BC

structure (Huang et al., 2017), and the first convolution layer of the network is also modified in the same way as in PreAct ResNet-18 for image size  $32 \times 32$ .

### A.5 TRANSFORMER-BASED SETTINGS AND RESULTS

In this section, we compare the performance of JPEG-DL compared to its baseline using the EfficientFormer-L1 model (Li et al., 2022) on CIFAR-100, as well as two fine-grained datasets, Flowers and Pets. We followed the experimental setup described by Xu et al. (2023), adhering to the same configurations mentioned in Table 5. The learning rate was set to 0.003 for CIFAR-100 and 0.005 for the fine-grained tasks, aligning with our standard settings in Section 4.

Interestingly, we found that the best performance for transformer-based architectures was achieved when the quantization tables were initialized with all ones, effectively representing the highest quality factor quantization table for JPEG. The top-1 validation accuracy performance is presented in Table 6, demonstrating the significant improvements achieved by JPEG-DL over the baseline.

Table 5: Hyper-parameter setting on EfficientFormer-L1.

Settings	CIFAR-100	Pets	Flowers
batch size	512	512	512
warmup epochs	50	100	100
training epochs	300	600	600

Table 6: Top-1 accuracy (%) on CIFAR-100 and two fine-grained image classification tasks using EfficientFormer-L1. We report the mean and standard deviation of the experimental results over three runs with different random seeds. The best results are indicated in bold, and values in parentheses indicate relative accuracy gains over the baseline.

Model	Method	Accuracy (%)
CIFAR-100	Baseline	80.27 $\pm$ 0.33
	JPEG-DL	<b>80.49</b> $\pm$ 0.23 (+0.22)
Flowers	Baseline	69.78 $\pm$ 0.33
	JPEG-DL	<b>73.05</b> $\pm$ 0.12 (+3.27)
Pets	Baseline	65.52 $\pm$ 1.23
	JPEG-DL	<b>69.28</b> $\pm$ 0.42 (+3.76)

### A.6 SENSITIVITY AND Q TABLE INITIALIZATION

Figure 10 presents the estimated sensitivity values for all models considered in the CUB200 dataset and a subset of models used for CIFAR-100, as proposed by Salamah et al. (2024b); Zheng et al. (2023). These estimated sensitivity values are used to initialize the quantization table for JPEG-DL. Figure 11 illustrates the initial and converged values of the quantization table at the end of training.

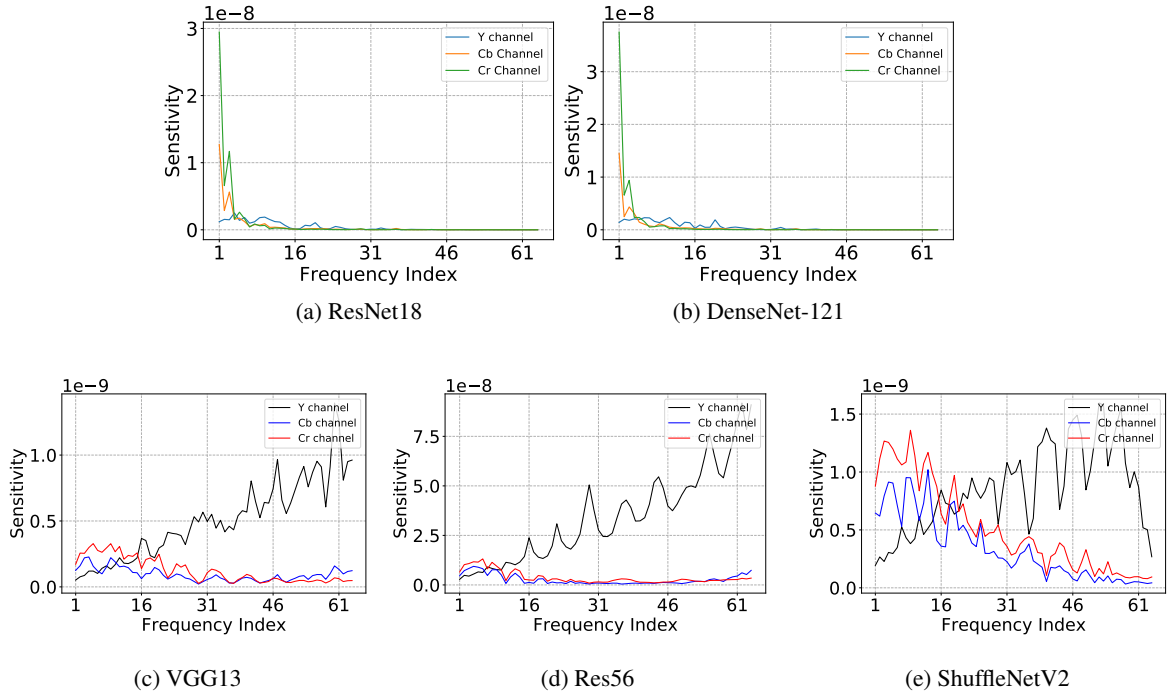


Figure 10: The estimated sensitivity is shown for two pre-trained models on the CUB200 (first row) and three pre-trained models on the CIFAR-100 (second row), with sensitivity indices arranged in the default zigzag order.

### A.7 FEATURE MAPS VISUALIZATION

Figure 12 presents the feature maps extracted after the first dense block in DenseNet-121 for both the JPEG-DL and the baseline models, trained on the Flowers dataset using the model from Table 2. The shown example was incorrectly classified by the baseline model, while the JPEG-DL model correctly classified it.

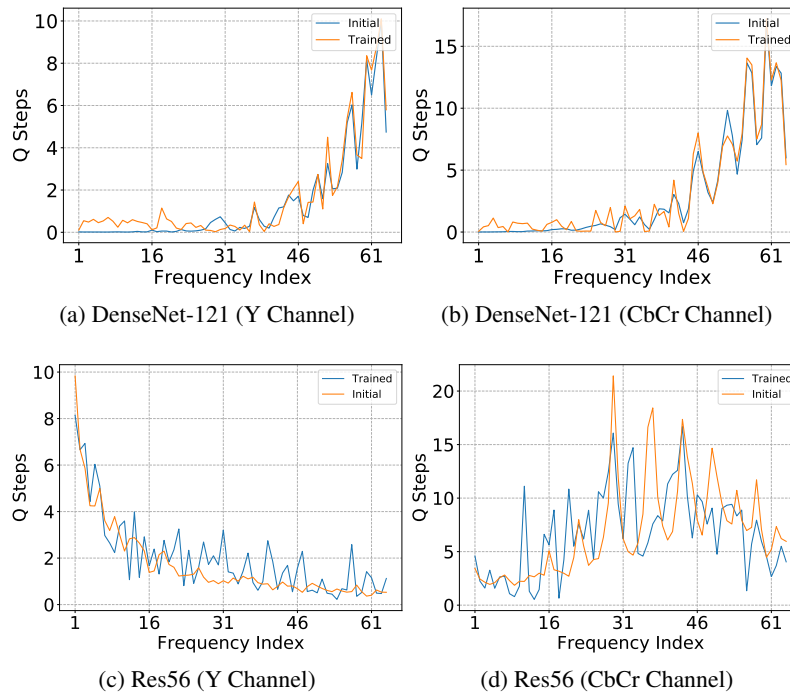


Figure 11: Initial and final quantization tables for Res56 trained on CIFAR-100 and DenseNet-121 trained on CUB200.

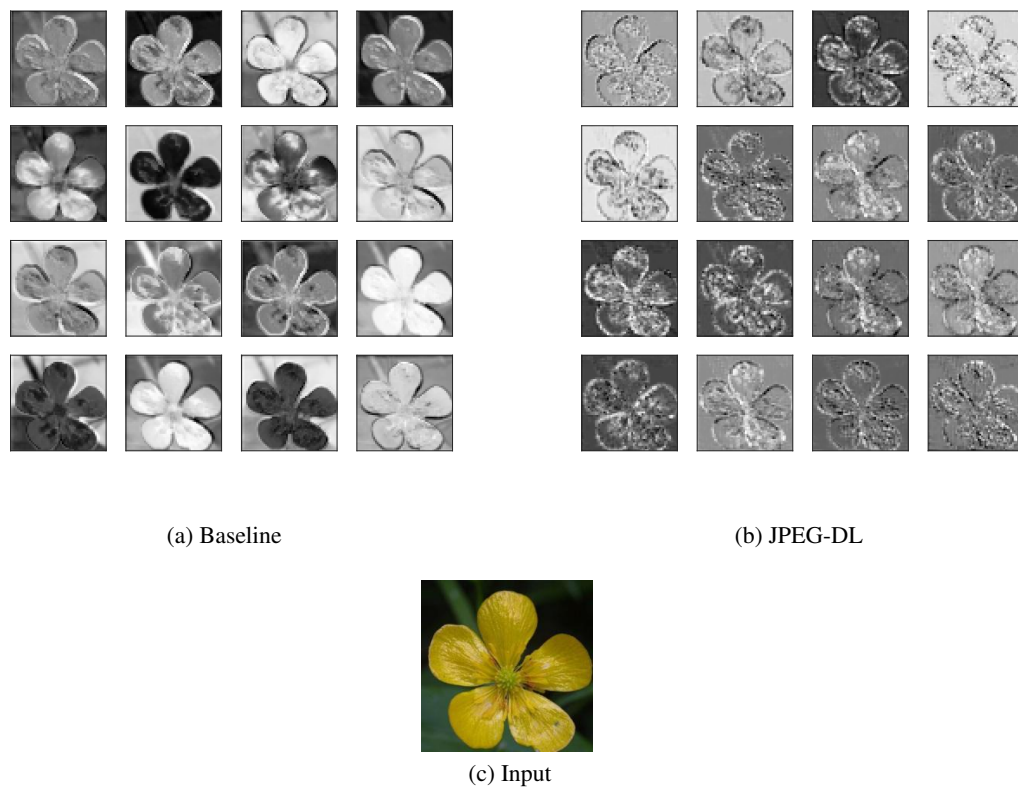


Figure 12: Feature maps of size 56x56 are shown after the first dense block in DenseNet-121 for both JPEG-DL and baseline models in Figs. 12a and 12b, respectively, using an original input shown in Fig. 12c. The JPEG-DL model highlights the foreground (flower) more distinctly, while the baseline model shows less contrast, contributing to its misclassification.